PHOTONICS Research

Subwavelength imaging and detection using adjustable and movable droplet microlenses

Xixi Chen,[1] Tianli Wu,[1] Zhiyong Gong,[1] Yuchao Li,[1,2] Yao Zhang,[1,3] and Baojun Li[1]

[1]Institute of Nanophotonics, Jinan University, Guangzhou 511443, China
[2]e-mail: liyuchao@jnu.edu.cn
[3]e-mail: zhyao5@jnu.edu.cn

Received 19 September 2019; revised 5 December 2019; accepted 14 December 2019; posted 18 December 2019 (Doc. ID 377795); published 5 February 2020

We developed adjustable and movable droplet microlenses consisting of a liquid with a high refractive index. The microlenses were prepared via ultrasonic shaking in deionized water, and the diameter of the microlenses ranged from 1 to 50 μm. By stretching the microlenses, the focal length can be adjusted from 13 to 25 μm. With the assistance of an optical tweezer, controllable assembly and movement of microlens arrays were also realized. The results showed that an imaging system combined with droplet microlenses could image 80 nm beads under white light illumination. Using the droplet microlenses, fluorescence emission at 550 nm from CdSe@ZnS quantum dots was efficiently excited and collected. Moreover, Raman scattering signals from a silicon wafer were enhanced by ∼19 times. The presented droplet microlenses may offer new opportunities for flexible liquid devices in subwavelength imaging and detection.

https://doi.org/10.1364/PRJ.377795

1. INTRODUCTION

Dielectric microspheres have been extensively exploited as promising materials for nano/microlens-assisted techniques in biophotonics and chemistry [1–8]. Applications of dielectric microspheres to enhance photon–matter interactions using several extraordinary optical properties (photonic nanojets [9,10], whispering-gallery modes [11], and directional antennas [12]) have been demonstrated, such as single molecule and nanoparticle detection [2,13], nanopatterning [14], signal enhancement [4,15–17], and performance improvement of optical systems [18–20]. Profiting from the ability of focus properties and near-field coupling of microspheres, subdiffraction imaging can also be achieved without fluorescent labeling [1,21]. Traditional microsphere-assisted lenses are usually placed directly onto specimen surfaces [1,19,22]. To improve the mobility of the microlenses, some methods have been proposed, such as fixing a microsphere at the end of a rod-shaped microstructure [23,24], a Janus microsphere lens as a microrobot that is powered by local catalytic reactions [25], and combining a microsphere with an atomic force microscope cantilever to improve the sensitivity of the detection system [26,27]. However, because the field of view is confined by the microsphere size [22] while the resolving ability degenerates with the increment of the microsphere diameter [28], single-microsphere lenses hold either a very limited field of view or poor resolution.

Methods to form microsphere arrays have recently been proposed to enhance the applicability of microsphere-assisted lenses. For example, by immersing self-assembled microsphere arrays into elastomers to form microsphere-embedded films [15,28], real-time biological imaging and enhanced Raman detection of multiple specimens can be achieved. Also, microsphere arrays patterned in a microfabricated well template have been employed for immunofluorescent detection in aqueous systems [29]. Although the microsphere arrays can overcome the dilemma of the field of view and the resolving ability, the arrays were usually fixed in a pattern on a substrate so that they face the challenge in flexible manipulation to selectively image and detect specific objects, especially when the objects are highly dispersed in a large area of the sample. Moreover, because most reported dielectric microspheres are composed of solid materials [SiO_2, polystyrene (PS), barium titanate glass, etc.], they have fixed focal lengths (L) and magnifications and, therefore, cannot be adjusted to image or detect objects that have diverse shapes, sizes, or multilayers.

With their ability to trap and manipulate small objects, optical tweezers (OTs) have become a powerful tool for noncontact assembly of multiple micro/nanostructures [30–34]. OTs have been successfully combined with single microspheres to achieve surface imaging [35] and near-field Raman imaging [3]. Assembly of microspheres by OTs avoids the use of any fixed patterns or substrates, and the manipulation is also effective to small droplets that can be deformed to act as adjustable microlenses.

In this work, we demonstrate adjustable and movable droplet microlenses of liquids with high refractive indices (n)

assembled and manipulated by OTs. The droplet microlenses are prepared by ultrasonic shaking in deionized water, and the L of the microlenses can be adjusted by horizontally stretching the droplets. Microlens arrays are assembled and manipulated with the assistance of OTs, and the magnification and effective numerical aperture (NA_{eff}) of the microlenses are investigated by direct imaging with label-free samples. The microlenses are also employed to excite and collect fluorescence emission from quantum dot (QD) clusters and to enhance Raman scattering signals from a silicon (Si) wafer. The results indicate that the presented method may help to develop flexible liquid devices for imaging and detection at a subwavelength scale.

2. RESULTS AND DISCUSSION

A. Droplet Preparation and Experimental Setup

The droplets used in this work were prepared by an emulsion process [36], as schematically depicted in Fig. 1(a). First, 1-bromonaphthalene ($C_{10}H_7Br$, 95%, 200 μL) was added dropwise into deionized water (1 mL) *in vitro* at 22°C. The mixture was then shaken in an ultrasonic bath at a frequency of 80 kHz for 5 min. $C_{10}H_7Br$ is usually used as a material of oil-immersion objective because of the high refractive index ($n = 1.66$), optical transparency (see Fig. 7 in Appendix A for the transmittance spectrum of $C_{10}H_7Br$), and chemical inertness. After that, the $C_{10}H_7Br$ was emulsified to form droplet microlenses in spheroids of different sizes in deionized water, with diameters (D) ranging from ~1 to ~50 μm [Fig. 1(b); see Appendix B for further details]. To investigate the focusing ability of the droplet microlenses, the experimental setup was constructed as schematically shown in Fig. 1(c). An optical microscope (Union, HISOMET II-DH II) with a CCD camera (Sony iCY-SHOT, DXC-S500) was used for morphological observation and measurements. The suspension of the droplet microlenses in water was added dropwise onto a glass slide placed on a translation stage. Two fiber probes (see Appendix C for the fabrication) were mounted on two tunable fiber positioners (precision, 50 nm), as shown in the inset of Fig. 1(c). The probe tips were introduced into the suspension and could be adhered to a targeted droplet microlens. By adjusting the fiber positioner, we could draw the probes sideways so that the droplet microlens was controllably stretched.

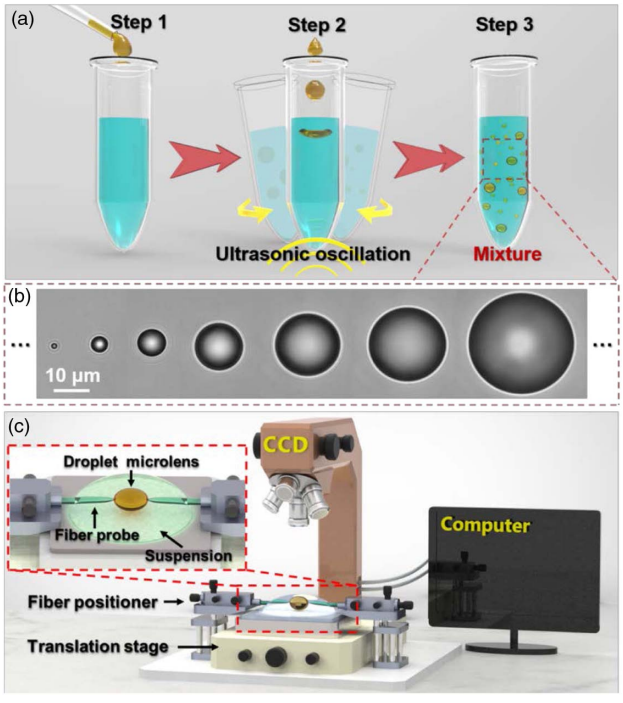

Fig. 1. Droplet preparation and experimental setup. (a) Preparation process of the droplet microlenses. (b) Optical microscope images of the droplet microlenses showing they are spheroids of different sizes. (c) Schematic of the experimental setup. The inset shows a schematic of the microlens deformation.

B. Focusing of the Droplet Microlenses of Different Sizes and Shapes

Direct observation of the focusing of the droplet microlenses was achieved via the Tyndall effect. A solution of PS nanoparticles (concentration, 44.2 mg/mL; diameter, 100 nm, 5 μL) was added dropwise onto the suspension of droplet microlenses (100 μL) on the glass slide. Laser beams at the wavelength of 473 nm were injected into an extra fiber probe (FP1) that was introduced into the suspension in the direction indicated by the blue arrow in Figs. 2(a1) and 2(b1). Output beams from the probe were used as the illumination to the targeted microlens. The size of the laser beam was approximately 10 μm, and the light beam was collimated by a fiber collimator. The distance between the probe tip and targeted microlens was 40 μm. For spherical targeted microlenses with diameters of 8, 12, and 16 μm, the focusing effect of incident light was directly observed at the rear of the microlens by injecting a beam with an intensity of 230 μW at 473 nm into the probe [Fig. 2(a)], revealing L of 8.1, 13.3, and 21.1 μm, respectively. The focal length was measured with an image processing method. First,

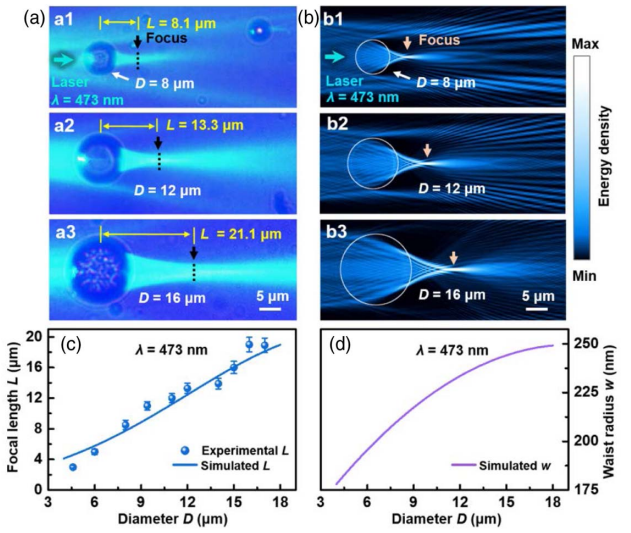

Fig. 2. Focusing of the droplet microlenses in different sizes. (a) Optical microscope images of microlenses with diameters D of (a1) 8, (a2) 12, and (a3) 16 μm. (b) Simulated energy density distribution for each microlens. (c) L as a function of D at a fixed wavelength of 473 nm. (d) Waist radius (w) as a function of D at a fixed wavelength of 473 nm.

the intensity of light spots of Figs. 2(a) was calculated by performing three-dimensional color mapping using MATLAB software. Then, the focal length was obtained by measuring the distance between the strongest intensity point on the optical axis of the focused beam and the center of the droplet microlens. The precision of the measurement was ±250 nm.

The focusing of the microlenses was also numerically investigated by simulations with a two-dimensional finite-element method (FEM, COMSOL Multiphysics 5.3); the corresponding field distributions are shown in Fig. 2(b). The FEM simulations were performed with the RF module of COMSOL Multiphysics 5.3. The refractive indices of the microlens and surrounding region were set as 1.66 and 1.33, respectively. A free triangular mesh with maximum element size of the incident wavelength $\lambda/7$ was set for the whole regions. A radiation boundary was set as the incident wave, and scattering boundary conditions were used for all other boundaries. From a series of FEM simulations, L as a function of D at a fixed wavelength (473 nm) was obtained [Fig. 2(c)]. The focal spot size of the output beam was described by the waist radius, which is half the diameter of the focal spot size and measured at $1/e$ from the maximum height. Waist radius (w) of each output beam from the microlenses was also determined, as shown in Fig. 2(d). At a fixed λ of 473 nm, smaller microlenses provide stronger light concentration [10]. In addition, the numerical aperture (NA) $= n \sin\theta$ of the objective lens, n is the refractive index of the object space, θ is half the maximum acceptance cone of the objective lens to the optical axis, and the subwavelength light confinement behind the microlens could be achieved with the high NA of droplet microlens with high refractive indices (n). Further, the output beams from the droplet microlenses converge into photonic nanojets as those generated by solid dielectric microspheres [9,13,37]. Note that the experimental data of the waist radius w can also be obtained via the microscope observation. However, the data of the waist radius w have a relatively large deviation because the light spot size is smaller than the input wavelength. To maintain the accuracy and credibility of this work, the experimental data of w were not included here.

To investigate the focusing of the droplet microlenses with different shapes, the targeted microlens was stretched into an ellipsoid by the fiber probes adhered to the droplet microlens (Fig. 3). The two probes (FP2 and FP3) were manipulated by the fiber positioners to simultaneously approach the upper and lower sides of a targeted spherical droplet microlens with a diameter of 12 μm [Fig. 3(a1)] until the probes were adhered to the microlens. Then, the spherical microlens, with a focal length of 13.3 μm at the incident wavelength λ of 473 nm, was vertically stretched into an ellipsoid with semimajor and semiminor axes of 7.1 and 5.5 μm, respectively [Fig. 3(a2)], and 8.6 and 5.0 μm [Fig. 3(a3)] by manipulating the probes via the fiber positioners. Correspondingly, the focal lengths L of the ellipsoidal microlenses at $\lambda = 473$ nm became 17.9 and 25.0 μm. In our experiments, the focal length of the targeted droplet microlens can be adjusted from 13.3 to 25.0 μm by this stretching method. For convenience, the lengths of the semimajor and semiminor axes of the ellipsoidal microlens are denoted by A and B, respectively, so that the ratio A/B represents

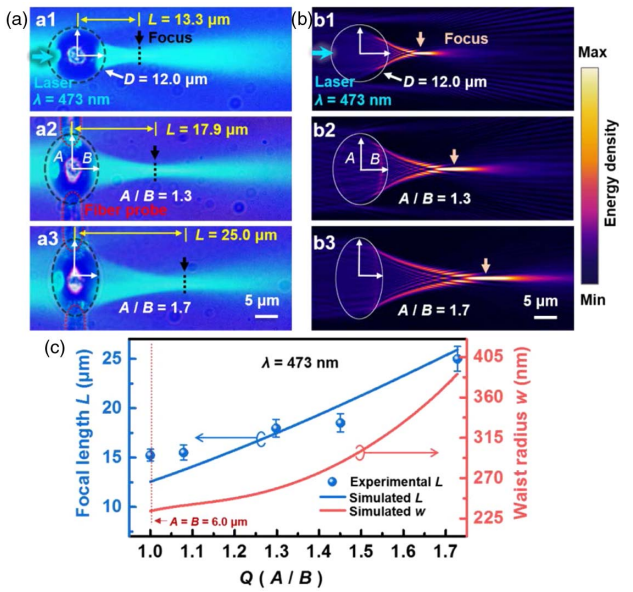

Fig. 3. Focusing of the droplet microlenses of different shapes. (a) Optical microscope images of microlenses with shapes of (a1) a sphere with a diameter D of 12 μm, (a2) an ellipsoid with a ratio between the semimajor and semiminor axes (A/B) of 1.3, and (a3) an ellipsoid with $A/B = 1.7$. (b) Simulated energy density distribution for each microlens. (c) Focal length L and waist radius (w) of the output beams as functions of A/B at a fixed wavelength of 473 nm.

the stretching extent of the microlens. The field distributions of the ellipsoidal microlenses were also obtained by FEM simulations [Fig. 3(b)], indicating that the focus shifts forward along the propagation direction with the increase of A/B. With FEM simulations, the focal lengths L and the waist radius w of the output beams as functions of A/B at a fixed wavelength (473 nm) were also obtained [Fig. 3(c)]. Note that when A/B reached above 1.5, the value of the w became larger than the incident wavelength (473 nm). Excessive stretching when the shape of the microlens changes from a sphere to an ellipsoid led to considerable divergence of the output beams and will slightly affect the detection and imaging performance of the microlens [37,38]. Fortunately, the change rate of the w is smaller than 0.12; thus, it will not influence obviously the imaging quality. Moreover, the effect of spherical aberration can be negligible here because the imaging region of the sample was located near the center of the microlens. In the center region, no spherical aberration was observed in our experiments. But it should be noted that the spherical aberration will occur near the outer edge of the microlens because of its relatively large curvature. Furthermore, the contacting points of the fiber probe were located at the edge of the droplet microlens, and it will not affect the imaging at the center region. Therefore, to minimize the effects from the spherical aberration and the contacting points of the fiber probes, the imaging sample should be placed near the center of the droplet microlens.

C. Assembly and Manipulation of Microlens Arrays

We used a multiple-optical-trap system (Tweez250si) to assemble and manipulate the droplet microlens arrays. A 60× water-immersion inverted objective (NA, 1.0) and glass chamber

containing the solution of the droplet microlenses were used in the experiments [Fig. 4(a)]. In our experiment, the droplet microlenses with size ranging from 1 to 35 μm could be always lifted by the OT. In this case, gravity and thermal (Brownian) forces are the only forces to be compensated by the OT because the microdroplets within this size range could suspend in the deionized water and without adhesion to the substrate. The height of the droplets was controlled by the OT. For larger microdroplets (diameter >35 μm), they will possibly deposit onto the surface of the substrate. To minimize the influence of substrate on the trapping stability, the surface of the substrate was modified with an oleophobic coating, which can effectively avoid the adhesion between the microdroplets and the substrate. To trap and manipulate the droplet microlenses with diameters D of 1–50 μm, the power of the trapping laser (at 1064 nm) was adjusted from 3 to 650 mW. The center of the optical potential well, i.e., the focus of the trapping laser beam, was moved to approach the droplet microlens. The targeted microlens was then attracted toward the center of the trapping light, and the gravity was counteracted by the optical trapping force [Fig. 4(b)]. With the optical traps created by the tweezers, the droplet movement was constrained within a certain region around the equilibrium point so that the Brownian motion was also sufficiently suppressed, resulting in stable trapping of the microlens (see Appendix D for the details of the Brownian motion of the optically trapped microlenses). Then, multiple optical traps arranged in an array were used to trap the microlenses and assemble them into a microlens array [Fig. 4(c)]. The microlens array was able to be manipulated by moving multiple optical traps. As an illustration, nine droplet microlenses with the same D (6.8 ± 0.2 μm) were assembled into a 3 × 3 array [Fig. 4(d); see Visualization 1 for further details]. Note that microlens arrays consisting of droplets in different sizes can also be assembled. For example, a 4 × 7 array of microlenses with D of 6.2–9.5 μm arranged in descending order was assembled and then shifted by moving the optical traps [Figs. 4(e) and 4(f)]. Two droplets (R1 and R2) that remained stationary at the bottom of the chamber were regarded as reference points. A detailed demonstration of the manipulation process is presented in Visualization 2. In addition, in the OTs system we used, 200 traps can be formed simultaneously by using the acousto-optic deflector (AOD). However, the maximum microlens array was limited by the optical power of the trapping laser and the observation field of the optical microscope. Therefore, in our experiments, the maximum element that can be manipulated is approximately 80 (with diameter of 10 μm). The flexible assembly and manipulation of the microlens arrays provide the possibility to image and detect objects in large areas and at different depths in samples.

D. Subwavelength Imaging

The droplet microlens was first applied to the imaging of the gratings of a Blu-ray Disk (BD) by an optical microscope

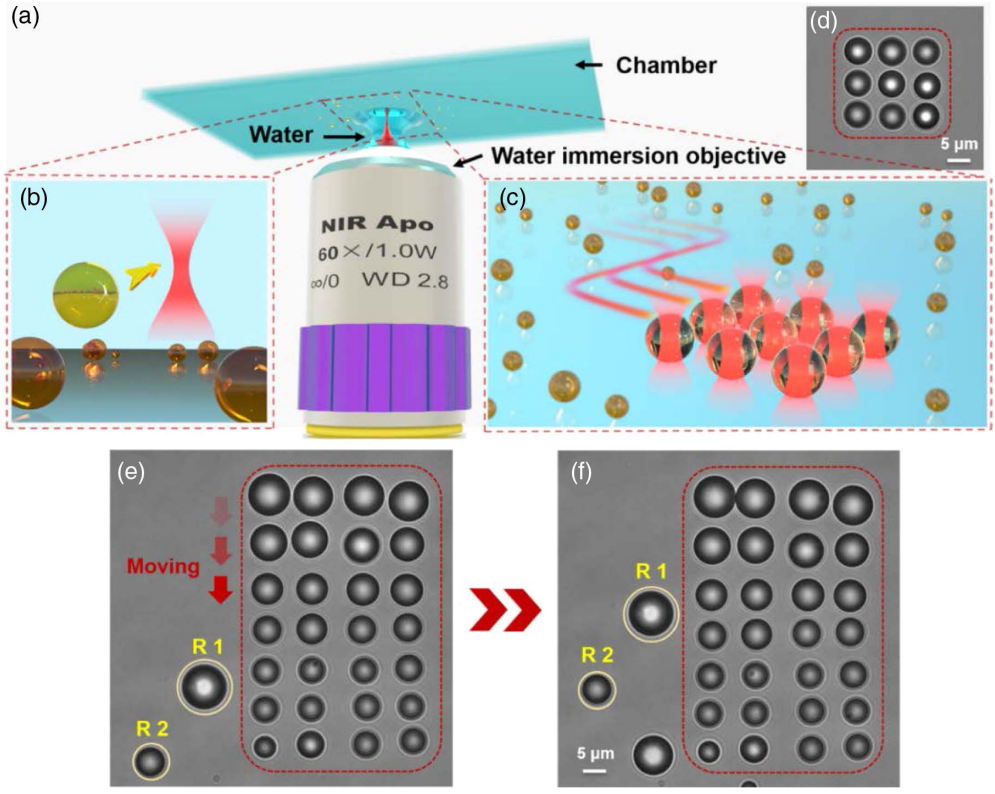

Fig. 4. Microlens array assembly and manipulation. (a) Schematic of the optical trapping and manipulation system. (b) Optical trapping of a single droplet microlens. (c) Optical trapping and manipulation of multiple droplet microlenses arranged in an array. (d) Optical microscope image of a 3 × 3 array of droplet microlenses with the same diameter D of 6.8 ± 0.2 μm. (e), (f) Shifting of a 4 × 7 array of microlenses with D of 6.2–9.5 μm arranged in descending order.

(Hirox, KH-7700; objective, OL-350 II; WD = 10.6 mm) without a tube lens, as depicted schematically in Fig. 5(a). Under illumination, near-field evanescent waves that carried high spatial frequency information of the sample are coupled into the droplet microlens and transformed into propagating waves for far-field observation [37,39]. In the experiments, the suspension of droplet microlenses was directly added dropwise onto the surface of a BD with the protective layer removed. The scanning electron microscopy (SEM) image of the disk shows that the gratings have a width of 200 nm and spacing of 100 nm [Fig. 5(b)]. Without the droplet microlenses in the field of view of the microscope, the gratings of the disk could not be resolved. With the presence of the droplet microlenses with D of 4.8, 7.7, and 13.6 μm, the peaks of adjacent gratings become discernible, and the measured distances between the adjacent peaks, i.e., the interval of the gratings (d), were 1.55 [Fig. 5(c)], 1.24 [Fig. 5(d)] and 1.19 μm [Fig. 5(e)], respectively. As the interval of the gratings was 300 nm, the corresponding magnifications of the droplet microlenses were thereby ~5.2×, ~4.1×, and ~4.0×. In the Rayleigh's criterion to distinguish two adjacent spots in an image, the peak-valley ratio R_{p-v} from the intensity profile of the image should be larger than 20% [40]. As for the results presented in Figs. 5(c)–5(e), the values of R_{p-v} are 51%, 45%, and 42% for the droplet microlenses with D of 4.8, 7.7, and 13.6 μm, respectively. Therefore, although the contrast of the image was reduced due to the presence of the solution, the minimum feature size of the optical system combined with the droplet microlenses was considered as better than 300 nm since the values of R_{p-v} were all higher than 20%.

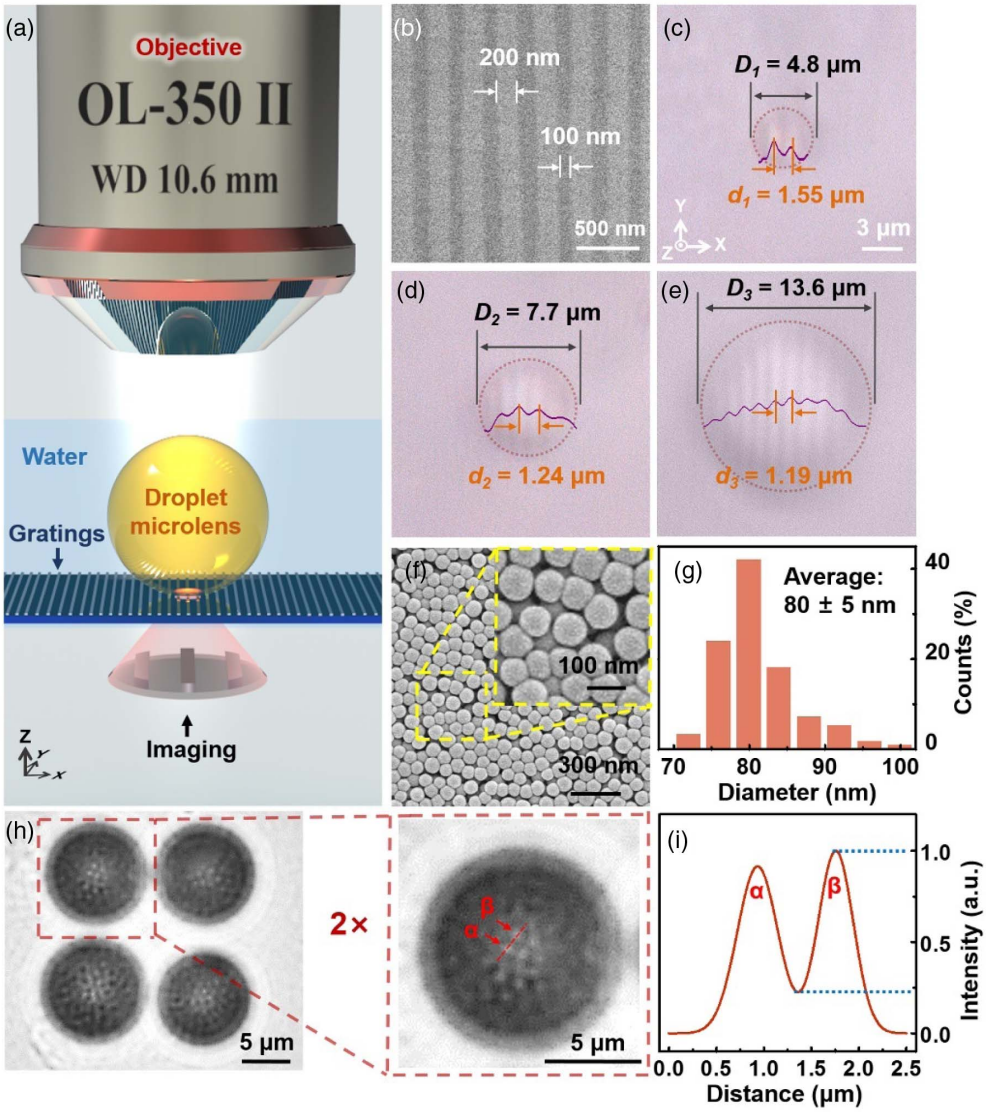

Fig. 5. Subwavelength imaging. (a) Schematic of subwavelength imaging with the droplet microlens. (b) SEM image of the gratings of a commercial Blu-ray Disk (BD). Optical microscope images of the BD gratings with the assistance of droplet microlenses with diameters of (c) 4.8, (d) 7.7, and (e) 13.6 μm. (f) SEM image of the stack of PS nanoparticle layers formed by evaporation-induced assembly. Inset is a magnified view of the PS nanoparticles. (g) Size distribution of the PS nanoparticles. (h) Optical microscope image of the PS nanoparticles obtained with the assistance of a 2 × 2 microlens array. The inset shows the magnified imaging of the view field of the droplet microlens. (i) Intensity variation of (h) along the transverse cross section through the center of two light spots (α and β) from the PS nanoparticles (D = 80 nm).

To further investigate the imaging performance, the droplet microlenses were also applied to the imaging of self-assembled PS nanoparticles. The optical microscope used in our experiment for imaging self-assembled PS nanoparticles has an inverted water-immersion objective (magnification = 60× and NA = 1.0). There was no tube lens in the optical system. And, the distance between the objective lens and samples was approximately 0.5 mm. The commercially available PS nanoparticles (diameter, 80 nm), which were formed into a stack of multiple layers by evaporation-induced assembly, were fixed on the inner of the cover of chamber [Fig. 5(f); see Appendix E for the preparation of samples]. The measured size distribution histogram showed that the particles possessed a diameter of 80 ± 5 nm [Fig. 5(g)]. A 2 × 2 array of the droplet microlenses ($D = 11.0 \pm 0.2$ μm) was assembled and then moved onto the surface of the stack of PS nanoparticles. Using the droplet microlenses array, the final image is a virtual image, which was obtained from the position above the inverted sample with a distance of approximately 3 μm, and the outlines of the PS nanoparticles became discernible in the field of view of the microscope [Fig. 5(h); see Visualization 3 for further details]. To further investigate the imaging ability in the presented method, we calculated the R_{p-v} for image of the array of 80 nm PS nanoparticles [Fig. 5(h)]. The result is 75% so that such a system combined with the droplet microlenses was able to image 80 nm beads. As the illumination of the OT system in our experiments was a halogen lamp with a peak wavelength λ of 550 nm, the subwavelength resolution can be achieved with the assistance of the droplet microlenses in the presented imaging system, which is attributed to the ability of subwavelength confinement of light as previously indicated by Figs. 2 and 3 and near-field collection.

E. Signal Enhancement

Inspired by the highly effective NA of ball lenses [41], we employed the droplet microlenses to enhance weak signals in detection as a further application. The microlenses were first applied to the enhancement of fluorescent signals from QDs. In the experiments, commercially available CdSe@ZnS QD clusters with an emission wavelength of 550 nm were dispersed on a SiO_2 slide [Fig. 6(a1); see Appendix E for the preparation]. The suspension of droplet microlenses was then dropped onto the QD sample on the slide. The microlenses with D of 11.8 [Fig. 6(a2)], 9.2 [Fig. 6(a3)], and 6.8 μm [Fig. 6(a4)] were separately moved right above the targeted QD cluster using the OT (see Visualization 4 for further details). The QDs were excited by the light through a bandpass filter (465–495 nm) from the mercury lamp of the microscope. The excitation light was converged by the inverted objective (60×, NA = 1.0, water immersion), and the optical power of the excitation light was ~620 μW. Without the microlenses, fluorescence emission from the QD cluster was rather weak and thereby can hardly be directly observed by the microscope [Fig. 6(b1)]. With the assistance of the droplet microlenses, the fluorescent signals were sufficiently enhanced and can be observed [Fig. 6(b2)–6(b4)]. Note that to achieve the strongest fluorescent signals, the droplet microlenses were vertically shifted along the Z axis to obtain the brightest fluorescence spots in the field of view. Profiles of the intensity distributions corresponding to the dark-field images were also obtained [Figs. 6(c1)–6(c4)], confirming that the fluorescent signals from the QDs were efficiently enhanced by the microlenses and that the smaller microlenses exhibited stronger enhancement than the larger ones. The signal collecting ability of the microlenses was evaluated by calculating the effective numerical aperture NA_{eff}. As in the experiments, we set a point source as the fluorescence from the QD cluster on a SiO_2 slide, and the height H of the microlens above the QD cluster was set as the focal lengths L to reach the maximum intensity of excitation [Fig. 6(d)]. In this case, NA_{eff} of the droplet microlens, expressed as $NA_{eff} = n \sin\theta$ [4], can be calculated by obtaining the collection angle θ for each microlens. The calculated NA_{eff} of the droplet microlenses with D of 11.8, 9.2, and 6.8 μm were 0.8, 0.84, and 0.87, respectively, indicating that the smaller microlens possessed a greater signal collecting ability as presented by the fluorescence intensities in Figs. 6(a)–6(c). Note that the power of the irradiating light (~620 μW) for exciting the QD cluster was much less than those required for bioimaging without the enhancement method [42,43], which lowers the risk of photodamage in signal detection *in vivo*.

Raman scattering signals can also be enhanced by the droplet microlenses. The suspension of droplet microlenses was directly dropped onto a Si wafer, and then the droplet microlenses sank to the bottom of suspension and close to the sample [Fig. 6(e)]. A Raman microspectrometer (Horiba, Xplora-Plus) with a 10× objective (NA = 0.25) was employed to obtain the Raman spectrum of the Si wafer with the excitation of a 785 nm laser (0.1 mW, spot size = 3.8 μm). For a bare Si wafer or regions of the wafer without the presence of the microlenses, the detected Raman signal was very weak. With the microlenses, the Raman signals of the Si wafer were sufficiently enhanced [Fig. 6(f)]. Similar to the case of enhancing the fluorescence from the QDs, the droplet microlenses acted on the convergence of both the excitation laser (785 nm) and the Raman scattering (wavelength, 818 nm; Raman shift, 520 cm^{-1}) from the Si wafer surface. Different from the case of QDs fluorescence enhancement, as the spot size of the 785 nm excitation laser (3.8 μm) was smaller than D of the microlenses (>4 μm), the microlenses sunk to the bottom of the solution and adhered to the Si wafer surface under the action of gravity to collect as much Raman signal as possible. With increasing D, the microlens was able to collect more Raman signal while the converging ability of the microlens became weaker due to the decreased NA_{eff}. In this case, the collected Raman signal was affected by both the microlens volume and NA_{eff}, resulting in an initial increase of the Raman intensity and then a decrease with increasing D (see Fig. 10 in Appendix F for further details). In our measurements, the maximum Raman intensity emerged at the microlens diameter of ~21 μm [Fig. 6(f)]. By subtracting the intensity of the Raman signals from the droplet microlens itself [44], an enhancement factor of ~19 can be obtained by using the ~21 μm droplet microlens compared with the signals from the bare Si wafer. In general, the enhancement of the signals of fluorescence and Raman scattering by the droplet microlenses in our experiments was attributed to the following: (i) the droplet microlenses converged the excitation lights (fluorescence, 465–495 nm; Raman, 785 nm) into beams with higher intensities to excite the samples [29]; (ii) emission of fluorescence

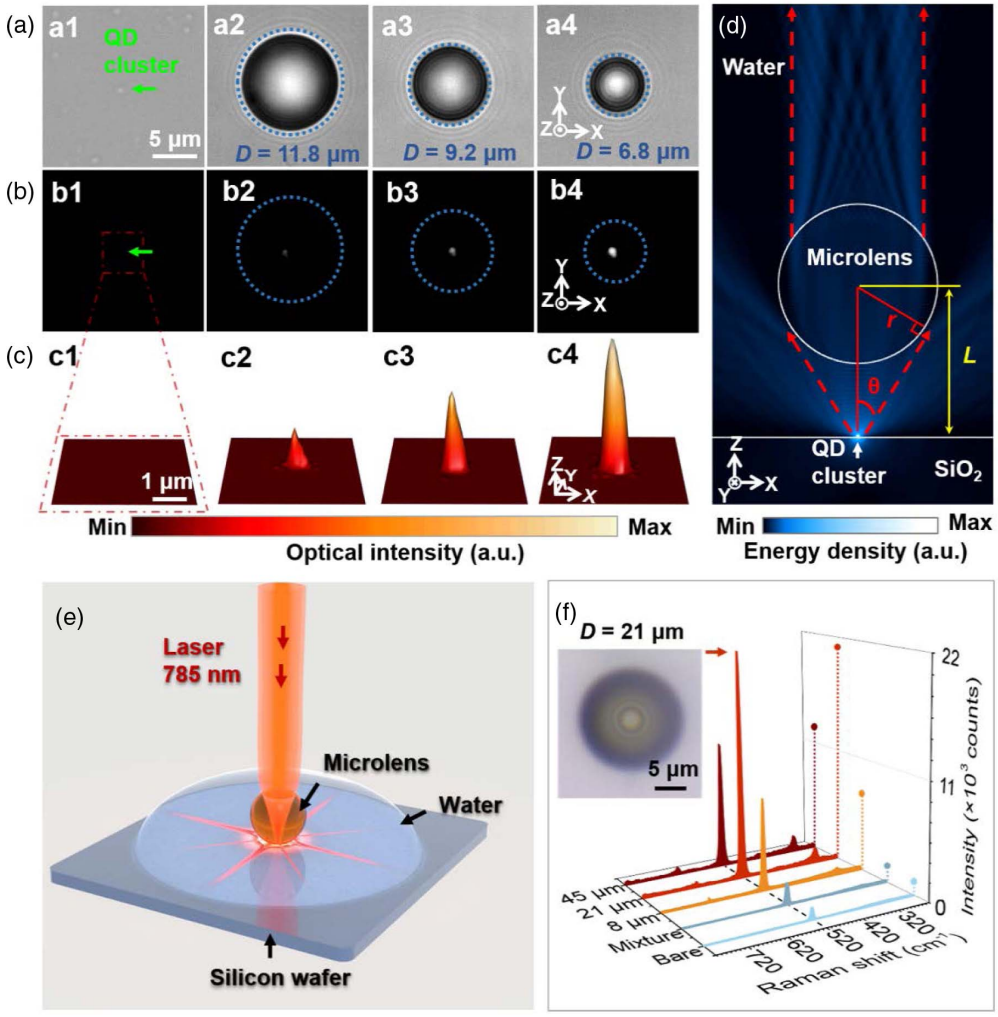

Fig. 6. Signal enhancement. (a) Optical microscope images of QD fluorescence enhancement. (a1) A QD cluster was located on the SiO_2 slide, and then microlenses with diameters D of (a2) 11.8, (a3) 9.2, and (a4) 6.8 μm were separately moved right above the QD cluster. (b) Fluorescence images of the QD cluster captured (b1) without and (b2)–(b4) with the assistance of microlenses. (c) Profiles of the intensity distributions corresponding to the dark-field images. (d) Illustration of the model used to calculate the effective numerical aperture NA_{eff}. (e) Schematic of the enhancement of Raman scattering signals from a silicon (Si) wafer. (f) Intensities of Raman scattering from the Si wafer without and with the assistance of the droplet microlenses with D of 45, 21, and 8 μm.

or Raman scattering was more efficiently collected by the droplet microlenses.

3. CONCLUSION

Adjustable and moveable droplet microlenses of $C_{10}H_7Br$ were prepared and demonstrated for applications in subwavelength imaging and detection. The droplet microlenses can be stretched by fiber probes to adjust the focal length. With the assistance of an OT, the microlens assays were flexibly assembled and moved to allow rapid scanning subwavelength imaging. Moreover, fluorescence from QDs and Raman signals from a Si wafer were efficiently enhanced by using the droplet microlenses. With the features of ease in preparation and assembly, adjustable focal length, mobility, and ability to enhance weak signals, the presented droplet microlenses are expected to find applications in liquid photonic devices for biomedical imaging and real-time detection in devices.

APPENDIX A: TRANSMITTANCE SPECTRUM OF $C_{10}H_7Br$

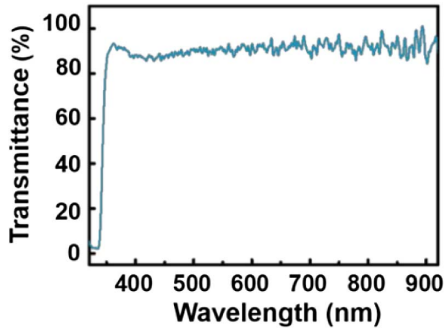

Fig. 7. Transmittance spectrum of 1-bromonaphthalene ($C_{10}H_7Br$) with the wavelength range from 300 to 900 nm.

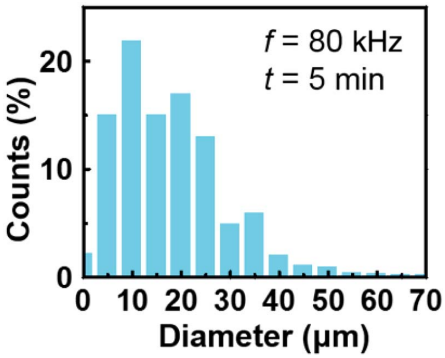

Fig. 8. The diameter distribution of the droplet at $f = 80$ kHz and $t = 5$ min.

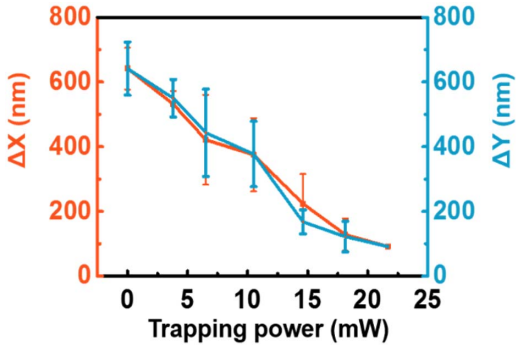

Fig. 9. Fluctuation region of Brownian motion of trapped microlens ($D = 1$ μm) as a function of trapping power.

APPENDIX B: DIAMETER DISTRIBUTION OF THE DROPLET

The droplet microlenses were prepared via ultrasonic shaking in deionized water, and their diameter was determined by the ultrasonic time (t) and frequency (f). As shown in Fig. 8, for $f = 80$ kHz and $t = 5$ min used in our experiments, the min and max diameters of the droplet microlenses were 1 μm and 50 μm, respectively.

APPENDIX C: FABRICATION OF OPTICAL FIBER PROBES

The fiber probes (FP1, FP2, and FP3) were fabricated by a flame-heating technique using single-mode optical fibers (core/cladding diameter, 9/125 μm; connector type, FC/PC; Corning Inc.). First, the buffer and polymer jacket of a fiber were stripped off to open a working window with a length of about 4 cm. The treated fibers were protected by a glass capillary (length, ~150 mm; thickness, ~0.1 mm; inner diameter, ~0.9 mm). Second, the bare fibers were heated by a flame for about 50 s to reach their melting point at an ambient temperature of 22°C. The heated fibers were drawn at rates of about ~10 mm/s (FP1) and ~5 mm/s (FP2 and FP3). The fibers broke to give fiber probes with different tips.

The fiber probes (FP1, FP2, and FP3) were fabricated by a flame-heating technique using single-mode optical fibers (core/cladding diameter, 9/125 μm; connector type, FC/PC; Corning Inc.). First, the buffer and polymer jacket of a fiber were stripped off to open a working window with a length of about 4 cm. The treated fibers were protected by a glass capillary (length, ~150 mm; thickness, ~0.1 mm; inner diameter, ~0.9 mm). Second, the bare fibers were heated by a flame for about 50 s to reach their melting point at an ambient temperature of 22°C. The heated fibers were drawn at rates of about ~10 mm/s (FP1) and ~5 mm/s (FP2 and FP3). The fibers broke to give fiber probes with different tips.

APPENDIX D: EFFECT OF BROWNIAN MOTION OF THE OPTICALLY TRAPPED DROPLET MICROLENSES

The criterion of the Brownian motion is the fluctuation region of the position of the trapped droplet microlens. The fluctuation region of the position of the trapped droplet microlens varies with the power of trapping laser and the diameter of droplet. For example, the fluctuation region of a trapped microlens with a diameter of 1 μm was approximately 100 nm in the x and y directions, which is much smaller than the input wavelength (~550 nm). For larger microlenses (e.g., 1 μm < diameter ≤ 50 μm), the fluctuation range becomes smaller because the Brownian motion is inversely related to the particle size. Besides, the Brownian motion could be further suppressed by increasing the trapping power, as shown in Fig. 9. Therefore, we consider that the effect of Brownian motion of the optically trapped microlenses can be neglected. Benefited from the minimized Brownian motion, the inference of light focusing (e.g., effective spot size) through the droplet was not observed in our image method [Fig. 5(h)].

APPENDIX E: PREPARATION OF SAMPLES FOR IMAGING AND SIGNAL ENHANCEMENT

The gratings used in Figs. 5(a)–5(e) were from a commercial BD. The surface of the BD was wiped with ethanol (99.9%). A square piece (2 cm × 2 cm) was sectioned from the BD with the protective layer (thickness, 100 μm) removed.

The stack of PS nanoparticle layers used in Figs. 5(f)–5(h) was formed by the evaporation-induced self-assembly of nanoparticles (Shanghai Huge Biotechnology Co.) with a diameter of 80 ± 5 nm. The nanoparticle suspension (41.6 mg/mL, 10 μL) was added dropwise into 99.9% ethanol (1 mL) at 22°C, and then the mixture was shaken in an ultrasonic bath at a frequency of 40 kHz for 15 min. The resulting suspension was added dropwise onto the inner side of the chamber cover, which was positively charged. The cover was held stationary in a dust-free environment for 1 h to provide a stack of PS nanoparticle layers through evaporation-induced self-assembly [45].

Commercially available water-soluble carboxyl CdSe@ZnS QDs (Zkwy Bio-tech Co., W-3600-550, 8 μmol/L) were used as a sample for signal enhancement. Deionized water (1 mL) was added to the QD solution (5 μL) at 22°C, and then the mixture was shaken in the ultrasonic bath at a frequency of 40 kHz for 10 min. The resulting solution was added dropwise onto the surface of a glass slide and held stationary in a dust-free environment for 4 h to form the QD clusters [Fig. 6(a1)] for the signal enhancement experiments.

APPENDIX F: DROPLET MICROLENS DIAMETER VERSUS RAMAN SCATTERING INTENSITY

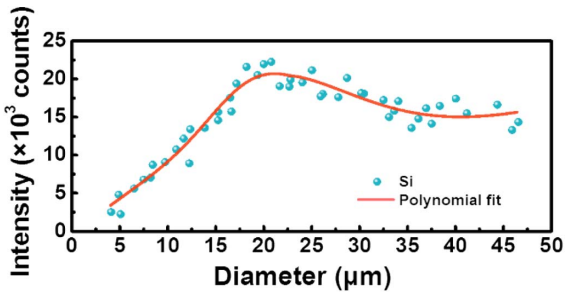

Fig. 10. Droplet microlens diameter versus intensity of Raman scattering signals. The fitting method is based on a polynomial fit.

Funding. National Natural Science Foundation of China (11874183, 61827822, 61905092); Fundamental Research Funds for the Central Universities (21619321).

Disclosures. The authors declare no conflicts of interest.

REFERENCES

1. Z. Wang, W. Guo, L. Li, B. Luk'yanchuk, A. Khan, Z. Liu, Z. Chen, and M. Hong, "Optical virtual imaging at 50 nm lateral resolution with a white light nanoscope," Nat. Commun. **2**, 218 (2011).
2. D. Gérard, J. Wenger, A. Devilez, D. Gachet, B. Stout, N. Bonod, E. Popov, and H. Rigneault, "Strong electromagnetic confinement near dielectric microspheres to enhance single-molecule fluorescence," Opt. Express **16**, 15297–15303 (2008).
3. J. Kasim, Y. Ting, Y. Y. Meng, L. J. Ping, A. See, L. L. Jong, and S. Z. Xiang, "Near-field Raman imaging using optically trapped dielectric microsphere," Opt. Express **16**, 7976–7984 (2008).
4. Y. C. Li, H. B. Xin, H. X. Lei, L. L. Liu, Y. Z. Li, Y. Zhang, and B. J. Li, "Manipulation and detection of single nanoparticles and biomolecules by a photonic nanojet," Light Sci. Appl. **5**, e16176 (2016).
5. J. Y. Lee, B. H. Hong, W. Y. Kim, S. K. Min, Y. Kim, M. V. Jouravlev, R. Bose, K. S. Kim, I. C. Hwang, L. J. Kaufman, C. W. Wong, P. Kim, and K. S. Kim, "Near-field focusing and magnification through self-assembled nanoscale spherical lenses," Nature **460**, 498–501 (2009).
6. W. Fan, B. Yan, Z. Wang, and L. Wu, "Three-dimensional all-dielectric metamaterial solid immersion lens for subwavelength imaging at visible frequencies," Sci. Adv. **2**, e1600901 (2016).
7. D. Kang, C. Pang, S. M. Kim, H. S. Cho, H. S. Um, Y. W. Choi, and K. Y. Suh, "Shape-controllable microlens arrays via direct transfer of photocurable polymer droplets," Adv. Mater. **24**, 1709–1715 (2012).
8. C. U. Murade, D. V. D. Ende, and F. Mugele, "High speed adaptive liquid microlens array," Opt. Express **20**, 18180–18187 (2012).
9. Z. Chen, A. Taflove, and V. Backman, "Photonic nanojet enhancement of backscattering of light by nanoparticles: a potential novel visible-light ultramicroscopy technique," Opt. Express **12**, 1214–1220 (2004).
10. S. Lecler, Y. Takakura, and P. Meyrueis, "Properties of a three-dimensional photonic jet," Opt. Lett. **30**, 2641–2643 (2005).
11. C. G. B. Garrett, W. Kaiser, and W. L. Bond, "Stimulated emission into optical whispering modes of spheres," Phys. Rev. **124**, 1807–1809 (1961).
12. P. Bharadwaj, B. Deutsch, and L. Novotny, "Optical antennas," Adv. Opt. Photon. **1**, 438–483 (2009).
13. X. Li, Z. Chen, A. Taflove, and V. Backman, "Optical analysis of nanoparticles via enhanced backscattering facilitated by 3-D photonic nanojets," Opt. Express **13**, 526–533 (2005).
14. E. Mcleod and C. B. Arnold, "Subwavelength direct-write nanopatterning using optically trapped microspheres," Nat. Nanotechnol. **3**, 413–417 (2008).
15. C. Xing, Y. Yan, C. Feng, J. Xu, P. Dong, W. Guan, Y. Zeng, Y. Zhao, and Y. Jiang, "Flexible microsphere-embedded film for microsphere-enhanced Raman spectroscopy," ACS Appl. Mater. Interfaces **9**, 32896–32906 (2017).
16. H. Aouani, P. Schön, S. Brasselet, H. Rigneault, and J. Wenger, "Two-photon fluorescence correlation spectroscopy with high count rates and low background using dielectric microspheres," Biomed. Opt. Express **1**, 1075–1083 (2010).
17. S. Lecler, S. Haacke, N. Lecong, O. Crégut, J. L. Rehspringer, and C. Hirlimann, "Photonic jet driven non-linear optics: example of two-photon fluorescence enhancement by dielectric microspheres," Opt. Express **15**, 4935–4942 (2007).
18. A. Devilez, B. Stout, and N. Bonod, "Compact metallo-dielectric optical antenna for ultra directional and enhanced radiative emission," ACS Nano **4**, 3390–3396 (2010).
19. H. Yang, N. Moullan, J. Auwerx, and M. A. M. Gijs, "Super-resolution biological microscopy using virtual imaging by a microsphere nanoscope," Small **10**, 1712–1718 (2014).
20. J. Wenger, D. Gérard, H. Aouani, and H. Rigneault, "Disposable microscope objective lenses for fluorescence correlation spectroscopy using latex microspheres," Anal. Chem. **80**, 6800–6804 (2008).
21. Y. Yan, L. Li, C. Feng, W. Guo, S. Lee, and M. Hong, "Microsphere-coupled scanning laser confocal nanoscope for sub-diffraction-limited imaging at 25 nm lateral resolution in the visible spectrum," ACS Nano **8**, 1809–1816 (2014).
22. A. Darafsheh, G. F. Walsh, L. D. Negro, and V. N. Astratov, "Optical super-resolution by high-index liquid-immersed microspheres," Appl. Phys. Lett. **101**, 141128 (2012).
23. A. Arya, R. Laha, G. M. Das, and V. R. Dantham, "Enhancement of Raman scattering signal using photonic nanojet of portable and reusable single microstructures," J. Raman Spectrosc. **49**, 897–902 (2018).
24. L. A. Krivitsky, J. J. Wang, Z. Wang, and B. Luk'yanchuk, "Locomotion of microspheres for super-resolution imaging," Sci. Rep. **3**, 3501 (2013).
25. J. Li, W. Liu, T. Li, I. Rozen, J. Zhao, B. Bahari, B. Kante, and J. Wang, "Swimming microrobot optical nanoscopy," Nano Lett. **16**, 6604–6609 (2016).
26. M. Duocastella, F. Tantussi, A. Haddadpour, R. P. Zaccaria, A. Jacassi, G. Veronis, A. Diaspro, and F. De Angelis, "Combination of scanning probe technology with photonic nanojets," Sci. Rep. **7**, 3474 (2017).
27. F. Wang, L. Liu, H. Yu, Y. Wen, P. Yu, Z. Liu, Y. Wang, and W. J. Li, "Scanning superlens microscopy for non-invasive large field-of-view visible light nanoscale imaging," Nat. Commun. **7**, 13748 (2016).
28. A. Darafsheh, C. Guardiola, A. Palovcak, J. C. Finlay, and A. Cárabe, "Optical super-resolution imaging by high-index microspheres embedded in elastomers," Opt. Lett. **40**, 5–8 (2015).
29. H. Yang, M. Cornaglia, and M. A. M. Gijs, "Photonic nanojet array for fast detection of single nanoparticles in a flow," Nano Lett. **15**, 1730–1735 (2015).
30. L. Paterson, M. P. MacDonald, J. Arlt, W. Sibbett, P. E. Bryant, and K. Dholakia, "Controlled rotation of optically trapped microscopic particles," Science **292**, 912–914 (2001).
31. A. Terray, J. Oakey, and D. W. M. Marr, "Fabrication of linear colloidal structures for microfluidic applications," Appl. Phys. Lett. **81**, 1555–1557 (2002).
32. J. E. Curtis, B. A. Koss, and D. G. Grier, "Dynamic holographic optical tweezers," Opt. Commun. **207**, 169–175 (2002).
33. L. Ikin, D. M. Carberry, G. M. Gibson, M. J. Padgett, and M. J. Miles, "Assembly and force measurement with SPM-like probes in holographic optical tweezers," New J. Phys. **11**, 023012 (2009).
34. P. J. Pauzauskie, A. Radenovic, E. Trepagnier, H. Shroff, P. Yang, and J. Liphardt, "Optical trapping and integration of semiconductor nanowire assemblies in water," Nat. Mater. **5**, 97–101 (2006).

35. M. Michihata, J. Kim, S. Takahashi, K. Takamasu, Y. Mizutani, and Y. Takaya, "Surface imaging technique by an optically trapped microsphere in air condition," Nanomanuf. Metrol. **1**, 32–38 (2018).
36. W. D. Bancroft, "The theory of emulsification, I," J. Phys. Chem. **16**, 275–309 (1912).
37. H. Yang, R. Trouillon, G. Huszka, and M. A. M. Gijs, "Super-resolution imaging of a dielectric microsphere is governed by the waist of its photonic nanojet," Nano Lett. **16**, 4862–4870 (2016).
38. P. K. Upputuri and M. Pramanik, "Microsphere-aided optical microscopy and its applications for super-resolution imaging," Opt. Commun. **404**, 32–41 (2017).
39. X. Hao, C. Kuang, X. Liu, H. Zhang, and Y. Li, "Microsphere based microscope with optical super-resolution capability," Appl. Phys. Lett. **99**, 203102 (2011).
40. M. Born and E. Wolf, *Principles of Optics* (Cambridge University, 1999).
41. Y. Matsuura, S. Kino, E. Yokoyama, T. Katagiri, H. Sato, and H. Tashiro, "Flexible fiber-optics probes for Raman and FT-IR remote spectroscopy," IEEE J. Sel. Top. Quantum Electron. **13**, 1704–1708 (2007).
42. J. K. Jaiswal, H. Mattoussi, J. M. Mauro, and S. M. Simon, "Long-term multiple color imaging of live cells using quantum dot bioconjugates," Nat. Biotechnol. **21**, 47–51 (2003).
43. Q. Ma, T. Y. Song, X. Y. Wang, Y. B. Li, Y. H. Shi, and X. G. Su, "Quantum dots as fluorescent labels for use in microsphere-based fluoroimmunoassays," Spectrosc. Lett. **40**, 113–127 (2007).
44. M. Arivazhagan and D. A. Rexalin, "Vibrational spectral analysis and first hyperpolarizability studies of 1-bromonaphthalene based on *ab initio* and DFT methods," Spectrochim. Acta Part A **83**, 553–560 (2011).
45. S. Kinge, M. Crego-Calama, and D. N. Reinhoudt, "Self-assembling nanoparticles at surfaces and interfaces," Chem. Phys. Chem. **9**, 20–42 (2018).